Development of Multi-Principal Element Alloys $W_{19.8}Mo_{19.8}Nb_{19.8}Ti_{19.8}Cr_{19.8}Al_1$ (At. %) Through Mechanical Alloying Process

Ágata Mayara Paula Pontes[a]* , Marcela Silva Lamoglia[a] , Leandro Bernardes Serrano[a],

Elioenai Levi Barbedo[a] , Antonio Augusto Araújo Pinto da Silva[a] , Geovani Rodrigues[a],

Gilbert Silva[a]

[a]Universidade Federal de Itajubá (UNIFEI), Itajubá, MG, Brasil.

Refractory multi-principal element alloys constitute a novel category of metallic materials, and they have good properties, particularly at elevated temperatures. Currently, casting and powder metallurgy stand as the two predominant manufacturing routes. This study focuses on the production of the $W_{19.8}Mo_{19.8}Nb_{19.8}Ti_{19.8}Cr_{19.8}Al_1$ (At. %) alloy via the mechanical alloying process. Analyses of morphology and particle size distribution at intervals of 12, 24, 36, and 48 hours of milling showed a gradual decrease in particle size according to increase in milling time. The XRD showed the presence of the BCC phase after 48 hours of milling, and the application of the Williamson-Hall methods indicated that after 12, 24, and 36 hours of milling, the crystallite size decreased and the microstrain increased gradually. However, after 48 hours of milling, there was an increase in these values, suggesting the reordering of the structure of this alloy. In addition, Fe contamination increases significantly for higher milling time.

Keywords: *Multi-principal element alloys, Mechanical alloying, Crystallite size, Williamson-Hall method.*

1. Introduction

The traditional concept of metallic alloy formation is that most of them are compounds by a main element, and could have solid or amorphous phases[1,2]. A new class of materials was discovered in 2004, known as high-entropy alloys (HEAs), and is described as alloys with multiple elements containing at least 5 main elements with an atomic percent between 5 and 35 At. %[3-6]. In these alloys, the high configurational entropy can stabilize solid solution phases with simple structures, such as BCC and FCC, compared to potentially fragile intermetallic phases[7,8]. Multi-principal element alloys (MPEAs) and complex concentrated alloys (CCAs) are new terms used in the HEAs field, where they have as alloy bases a mixture of multiple elements and avoid definitions about the number or composition of the elements or the number of phases formed, i.e., can have any number of solid solutions and intermetallic phases[6]. In addition, definitions of high configurational entropy are not very important and also allow non-metallic elements, expanding the field of application for these alloys[6,9]. In 2010, Senkov developed 2 refractory alloys with the elements composition W–Nb–Mo–Ta and W–Nb–Mo–Ta–V. These alloys exhibited promising properties at elevated temperatures, including a high melting temperature exceeding 2500 °C and an elastic modulus of 405 MPa at 1600 °C[10,11]. However, these alloys exhibited certain limitations, such as low ductility at room temperature, high density, and susceptibility to oxidation and corrosion[12]. To enhance the competitiveness of the refractory

alloys, elements such as Ti, Al, Zr, Cr, and Si are incorporated to reduce the density and improve properties such as oxidation and corrosion resistance[13]. Examples of these enhanced alloys include TaNbMoCrTiAl[7], CrMoNbTiW[14], and NbZrTiCrAl[15].

Among the majority of multi-principal element alloys, approximately 95% have been produced through casting methods, with subsequent annealing heat treatment or homogenization. Alternative techniques that have been employed include rapid solidification or mechanical alloying (MA)[16]. MA, in particular, proves to be advantageous for alloys containing high melting point metals, which are challenging to process via conventional casting methods. Furthermore, it is worth noting that the MA process has the additional benefit of increasing configurational entropy within the alloy. This enhancement contributes to the stability of the solid solution[4].

The Mechanical Alloying process is employed for the synthesis of both equilibrium and non-equilibrium phases in powder processing, achieved through high-energy milling. This method allows the production of homogeneous materials from mixed elemental powders[17,18]. However, it is necessary specific precautions to prevent contamination and oxidation during the milling process. For instance, contamination with Fe typically arises from the milling balls or grinding mills[13,17,19] and is often observed in alloys with a high concentration of W. Additionally, interstitial contamination, often by O and N, may result from the presence of process control agents (PCA). This is particularly common in highly reactive alloys containing elements such as Ti and Zr[13].

*e-mail: agatapontes@unifei.edu.br

Multi-principal element alloys containing refractory metals, when processed through MA, offer a distinct advantage by exhibiting enhanced microstructural homogeneity, thereby averting common defects, including phase segregation. The solid-state processing methodology employed in MA facilitates the fabrication of alloys comprising multiple elements with varying melting points, thereby contributing to a reduction in energy consumption during processing, especially when compared to the casting method for the production of high-melting-point alloys[20]. Some refractory multi-principal element development through the MA process exhibited interesting results; for example, the CrMoNbWTi alloy showed an ultra-high strength, 4345 MPa, and hardness of 11.88 GPa[21], and the TiZrNbMoTa alloy exhibited strain and rupture resistance values of 3759 MPa and 12.1%, respectively[22].

The refractory metals selected for the MPEA in this work were W, Mo, and Nb due to their high melting points; Ti was included to reduce density and also has high melting point; and Cr to enhance oxidation resistance. The addition of Al was suggested because it aids in reducing density and enhancing oxidation, and corrosion resistance, despite its tendency to form brittle intermetallic phases, depending amount added[23-26]. This work has focused on the development of the $W_{19.8}Mo_{19.8}Nb_{19.8}Ti_{19.8}Cr_{19.8}Al_1$ (At. %) refractory multi-principal element alloy through the MA process with elements that contain different melting points and investigated the milling influence on phase stabilization of this alloy.

2. Experimental Procedure

2.1. Thermodynamic Calculation (CALPHAD)

Thermodynamic calculations were performed using Thermo-Calc® software[27] and the TECHEA4 database to determine phase equilibrium and phase compositions for the alloy $W_{19.8}Mo_{19.8}Nb_{19.8}Ti_{19.8}Cr_{19.8}Al_1$ (At. %) studied in this work.

2.2. Alloy preparation

The $W_{19.8}Mo_{19.8}Nb_{19.8}Ti_{19.8}Cr_{19.8}Al_1$ (At. %) alloy was prepared with high-purity powder elements Al, Cr, Mo, Nb, Ti, and W and weighted in the aimed composition with a total ~30 g mass using an analytical scale (0.1 mg precision).

Information about the alloy atomic composition, purity, and particle size of the powders is shown in Table 1.

The mixed of raw powders were synthesized using a high-energy planetary milling NOAH-NQM-2 under an Ar atmosphere to avoid oxidation at 400 rpm speed for 48 h with a ball-to-powder weight ratio (BPR) of 15:1. The milling

balls and bowl used in this experiment were made of stainless steel. To avoid excessive cold welding of the powders, it was used 3 Wt. % of methanol (0.9 g) as a process control agent (PCA). The powders of the samples were characterized after milling for 12, 24, 36, and 48 hours. The parameters adopted to assist this work were related to other studies developed in refractory multi-principal element alloys processed through mechanical alloying, such as[16,21,28-34].

2.3. Alloy characterization

Crystallographic analysis of the samples after milling for 12, 24, 36, and 48 hours were performed via powder X-ray diffractometry (XRD) using a Panalytical model X'Pert Pro with Cu Kα (λ = 0.1542 nm) radiation. The diffraction angle (2θ) ranged from 30 to 90°, with a step size of 0.02° and a counting time of 1s per step. Identification of the different phases was performed using the PowderCell software[35] and crystallographic data from Villars and Calvert[36]. Rietveld refinement of XRD patterns was performed using the GSAS2 software program. The Williamson-Hall method was used to calculate the crystallite size and microstrain of the milled powders, applying the Uniform Stress Deformation Model (USDM)[37].

The morphology of the particles was characterized using an EVO MA15 Zeiss Scanning Electron Microscope (SEM in the backscattered electron (BSE) mode and an Energy Dispersive Spectrometer (EDS) (BRUKER/ XFlash 6l10) coupled to the SEM. The ImageJ software was employed to measure the particle size of the samples. The analysis was conducted by converting pixels to microns. Particles of varying sizes (small, medium, and large) were selected for measurement, and analyzed for each milling time (12, 24, 36 and 48 hours).

The particles size distribution after milling for 12, 24, 36, and 48 hours were determined using Microtrac ® Bluewave S3500 laser granulometer.

3. Results and Discussion

3.1. Thermo-Calc Calculation

Thermodynamic calculations using Thermo-Calc software were performed to predict the phases formed under equilibrium temperatures from the liquidus temperature to 300 °C, Figure 1 shows the mole fractions of the stable phases in this temperature range for $W_{19.8}Mo_{19.8}Nb_{19.8}Ti_{19.8}Cr_{19.8}Al_1$ (At. %).

Thermo-Calc software shows the BCC disordered phase as the primary precipitate from liquidus until 1200 °C and starts stabilizing the secondary phase compounded by a minor fraction of the C14-Laves phase. However, at lower

Table 1. Powder element information of the $W_{19.8}Mo_{19.8}Nb_{19.8}Ti_{19.8}Cr_{19.8}Al_1$ (At. %) alloy.

Elements	At. %	Purity (Wt. % min.)	Particle size (μm)	Supplier
Al	1.0	99.9	3 to 10	Alcoa Brasil ®
Cr	19.8	99.5	< 45	Sigma Aldrich
Mo	19.8	99.9	< 5	Sigma Aldrich
Nb	19.8	99.9	2 to 20	USP-Lorena
Ti	19.8	99.5	Up to 150	Sigma Aldrich
W	19.8	99.9	50 to 250	Sigma Aldrich

Development of Multi-Principal Element Alloys W$_{19.8}$Mo$_{19.8}$Nb$_{19.8}$Ti$_{19.8}$Cr$_{19.8}$Al$_1$ (At. %) Through Mechanical Alloying Process

3

temperatures, we observed stabilization of the μ phase at 800 °C and the transformation of the C14-Laves phase into C15-Laves phase around 470 °C, followed by a decrease in amount of the BCC phase. Table 2 summarizes the crystallographic information for the stable solid phases predicted by Themo-calc calculations for the W$_{19.8}$Mo$_{19.8}$Nb$_{19.8}$Ti$_{19.8}$Cr$_{19.8}$Al$_1$ (At. %) alloy.

Table 3 shows the chemical composition of the BCC, C14-Laves, and μ phases at 700 °C, indicating that elements with high melting points, such as W, Mo, and Nb, are more concentrated in the BCC disordered phase, in contrast to the C14-Laves phase, which has a lower concentration of these elements but highlights high Cr, Ti and Al contents, and the μ phase is rich in W and Cr.

Previous thermodynamic calculations were performed with varying Al atomic concentrations ranging between 1 and 5 At. %. These calculations revealed that even a minor addition of Al resulted in significant changes. Specifically, the introduction of Al led to an increase in intermetallic phases, such as μ, while simultaneously reducing the amount
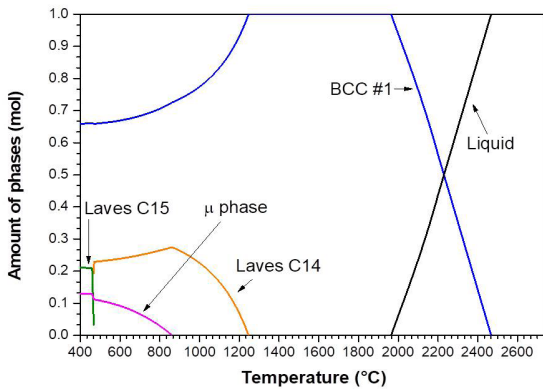

Figure 1. Calculation of phase fraction vs temperature diagrams (calculated in equilibrium) of the W$_{19.8}$Mo$_{19.8}$Nb$_{19.8}$Ti$_{19.8}$Cr$_{19.8}$Al$_1$ (At. %) alloy.

of the BCC phase. Additionally, it was observed that the system's melting point decreased with the inclusion of Al. Consequently, based on these findings, a composition containing 1 At. % Al was selected.

3.2. Morphologies analysis and granulometric distribution

Figure 2 shows micrograph of the W$_{19.8}$Mo$_{19.8}$Nb$_{19.8}$Ti$_{19.8}$Cr$_{19.8}$Al$_1$ (At. %) alloy, and the respective granulometric size after different milling times (12h, 24h, 36h, and 48h).

The micrograph of the W$_{19.8}$Mo$_{19.8}$Nb$_{19.8}$Ti$_{19.8}$Cr$_{19.8}$Al$_1$ (At. %) alloy (Figure 2a) after 12 hour milling process reveals particles with angular e irregular shapes. Additionally, large particles are observed, while smaller particles tend to flatten and cluster. According to[17,39] during the initial milling stages, characterized by high-energy collisions between powder particles, fragile particles experience fracture, while ductile particles undergo deformation, resulting in irregular morphologies

After 24 hour milling process (Figure 2c) the particles have diverse morphologies, including angular and rod-shaped structures, the powder morphologies are detailed at[20]. The particles that tend to cluster are likely to result from intense plastic deformation during milling. Following 36 hours of milling (Figure 2e), it is possible to observe a reduction in particle size, indicating work hardening followed by fracture of the powder particles during the milling process.

Upon reaching 48 hours of milling (Figure 2g), there is an increase in the quantity of smaller particles since there is a trend towards fracture over cold welding, where particles more commonly break into smaller pieces than undergo cold welding fractured particles. The stages of the MA process are thoroughly explained by[17]. However, some particles still cluster.

The particle size analysis (Figures 2b, d, e, f, and h) corresponds to the micrographs after 12, 24, 36, and 48 hours of milling, respectively, and were measured using the ImageJ software. It is observed that particles are larger after 12 hours of milling compared to those after 48 hours, indicating that

Table 2. Crystallographic information[38] of the solid phases predicted to be stable (by Themo-calc calculation) in temperatures between 300 and 2500 °C for the W19.8Mo19.8Nb19.8Ti19.8Cr19.8Al1 (At. %) alloy.

Phase	Strukturbericht designation	Pearson Symbol	Prototype	Space group
BCC	A2	cI2	W	Im3m
C14–Laves	C14	hP12	MgZn$_2$	P63/mmc
C15-Laves	C15	cF24	Cu$_2$Mg	Fd3m
μ	D8$_5$	hR13	Fe$_7$W$_6$	hR13

Table 3. Phase's chemical composition and volume fraction of the W19.8Mo19.8Nb19.8Ti19.8Cr19.8Al1 (At. %) alloy at 700 °C.

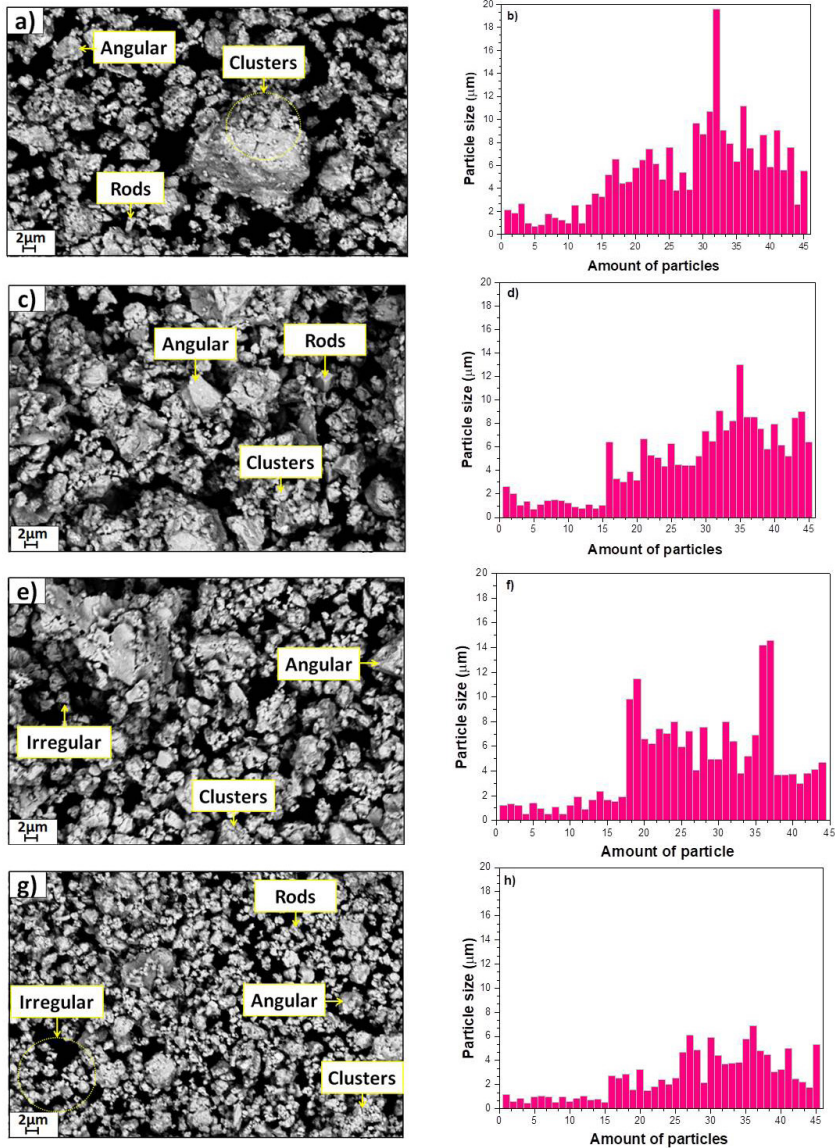| Phase	Volume fraction	Chemical elements					
	(Vol. %)	W	Mo	Nb	Ti	Cr	Al
BCC	0.74	0.2542	0.2640	0.2619	0.1990	0.020	0.0009
C14-Laves	0.19	0.0172	0.0343	0.0690	0.2479	0.6143	0.0172
μ	0.07	0.3006	0.1353	0.02574	0.000003	0.4614	0.0769

Figure 2. SEM Micrograph of the $W_{19.8}Mo_{19.8}Nb_{19.8}Ti_{19.8}Cr_{19.8}Al_1$ (At. %) alloy for milling times a) 12, c) 24, e) 36, and g) 48 hours and their respective particle size (b, d, f and h).

the milling process tends towards plastic deformation, cold welding, and particle fracture.

To validate and reinforce the particle sizes determined by the ImageJ software, an expanded sampling was examined. This analysis unveiled the granulometric particle distribution, depicted in Figure 3a-d), corresponding to milling durations of 12, 24, 36, and 48 hours, respectively. The analysis reveals a trimodal distribution, with a trend toward decreasing particle size as milling time increases. After 12 hours of milling, it was observed that there was a predominance of large particles (~62%) and minor percent (10%) with small particles, 3 and 4 µm. The percentage of particles measuring above 10 microm increases from approximately 50 to 85% for milling times between 12 and 36 hours. For milling times between 36 and 48 hours, there is a percent increase (~38%)

in smaller particles, with 2.5 µm in size, and a reduction (~60%) in particles measuring 10 µm. This shift suggests the fracture tendency is prevailing, indicating that the milling process promotes particle comminution and deformation, resulting in a finer particle size distribution.

The discrepancy in particle size measurement between the two methodologies lies in their specific approaches. ImageJ analysis is only based on SEM micrographs, yielding smaller particle sizes. In contrast, laser granulometric analysis provides more extensive sampling, resulting in a higher particle count.

The EDS analysis presented in Table 4 provides the chemical composition for milling of 12, 24, 36, and 48 hours. The results indicate significant contamination with iron (Fe). This contamination can be attributed to the
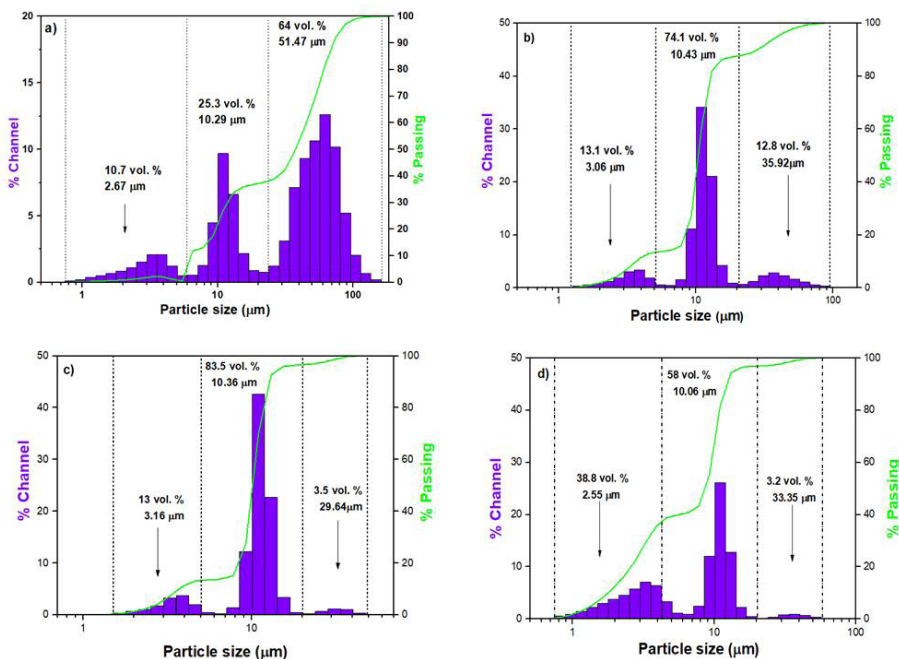
Development of Multi-Principal Element Alloys $W_{19.8}Mo_{19.8}Nb_{19.8}Ti_{19.8}Cr_{19.8}Al_1$ (At. %) Through Mechanical Alloying Process

5

Figure 3. Granulometric particle distribution of the $W_{19.8}Mo_{19.8}Nb_{19.8}Ti_{19.8}Cr_{19.8}Al_1$ (At. %) alloy after milling for 12, 24, 36 and 48 hours.

Table 4. Chemical composition of the MPEA $W_{19.8}Mo_{19.8}Nb_{19.8}Ti_{19.8}Cr_{19.8}Al_1$ (At. %) after 12, 24, 36 and 48h of milling time, measured by EDS.

Chemical elements (At. %)						
W	Mo	Nb	Ti	Cr	Al	Fe
22.4	14.4	14.9	18.2	18.9	1.2	9.9
23.3	11.2	10.9	15.6	18.0	1.0	19.9
21.6	9.8	9.8	13.5	15.3	1.4	28.6
17.4	11.8	12.7	15.6	20.0	1.10	21.4

experimental parameters utilized in this study, such as the BPR of 15:01 and a rotational speed maintained at 400 rpm. These parameters intensify collisions between the milling balls and powder particles, consequently increasing the level of Fe contamination. Notably, the highest level of Fe contamination, reaching approximately 28 At. %, was observed after 36 hours of milling, suggesting a potentially elevated degree of contamination within the scanned area. Previous research[40] has demonstrated that prolonged milling leads to the introduction of lattice defects, particularly vacancies. Moreover, the powder's high Fe contamination level increased with higher BPR and rotational speed.

According to Suryanarayana[17] during MA, the particles are trapped on the balls milling, causing severe plastic deformation and new surfaces are created due to the fracture of the particles. Also, the collisions between the milling balls and bowl result in the incorporation of these contaminations into powder particles. This contamination tends to increase if there is an increase in the milling time, ball-to-powder weight ratio (BPR), speed, etc. To minimize contamination, one way is to use media milling with the same material as the alloy being milled, or, as a general rule, milling balls and bowls should be harder or stronger than the powder being milled. For this reason, alloys with W have

high level of contamination from Fe in the MA, the milling medium is made by steel, which is softer than W.

3.3. X- ray diffractometry

The diffraction peaks resulting from the mixed powders (W, Mo, Nb, Ti, Cr, and Al) of the $W_{19.8}Mo_{19.8}Nb_{19.8}Ti_{19.8}Cr_{19.8}Al_1$ (At. %) alloy before and after 12, 24, 36, and 48 hours of milling time are shown in Figure 4. After 12 hours of milling, the diffraction peaks of the metal powders disappeared staying the diffraction peaks corresponding to the BCC structure (W prototype, Strukturbericht designation A2), suggesting the solubilization preference of elements such as Mo, Nb, and Ti in the lattice of W element, during the MA process, the atoms of others elements substitute gradually the position of the W to form substitutional solid solution with BCC structure. However, there is a minor fraction of diffraction peaks related to Cr element (BCC phase). According to study made by[14] these residual peaks in the XRD pattern can be due to the positive enthalpy of mixing with Mo and W, which indicates their limited solid solubility at room temperature. Due to the low concentration of the Al element, less than 3 Wt. %, X-ray diffraction probably did not detect it, and the Al peaks overlapped with those of Nb, Ti, and Cr.
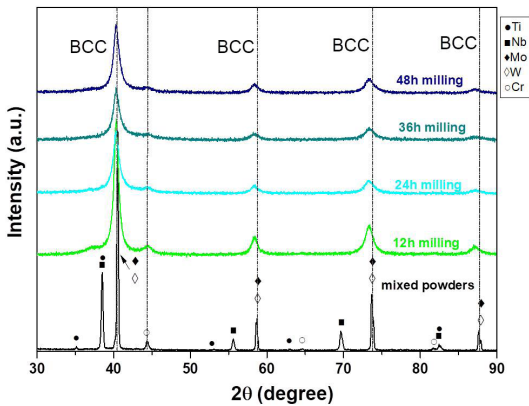
Figure 4. XRD of the $W_{19.8}Mo_{19.8}Nb_{19.8}Ti_{19.8}Cr_{19.8}Al_1$ (At. %) milling for 12, 24, 36 and 48hours and the diffraction of the mixed powder (W, Mo, Nb, Ti, Cr, and Al).

Figure 5. Diffraction of the main BCC peaks compared with W and Mo mixed powder in an interval from $2\theta = 38$ to $43°$.

Elemental inter-diffusion after milling between atoms with different lattices occurs when the energy barriers are overcome. When the atoms leave the original lattice position, the energy barriers are related to binding energy, and when the atoms occupy a new site, the energy necessary is related to the compatibility between the elements[17,40]. Therefore, elements within the same group, such as W and Mo, exhibit higher compatibility, facilitated by their shared BCC structure, promoting inter-diffusion.

After 24 and 36 hours of milling, observed a decrease in the crystallinity of the main peaks associated with the solid solution exhibiting a BCC phase, which can indicate a lattice deformation due to the MA process, especially at 36 hours, that exhibits higher broadening. This broadening implies a tendency for the alloy to become amorphous. Moreover, residual peaks correspond to Cr (BCC phase), suggesting incomplete mixing or diffusion of them into the alloy.

After 48 hours of milling, the BCC peaks intensified, indicating an enhancement in the crystallinity of the alloy. The observed changes at 48 hours can be attributed to the high-speed collisions between the milling balls and the milling bowl. These high-energy collisions result in an elevation of energy in the system, which may contribute to the stabilization of the BCC structure.

Figure 5 shows detailed diffraction of the main BCC peaks, compared with W and Mo raw powder (due to the similar crystalline structure their peaks overlap) within an interval from $2\theta = 38$ to $43°$. This interval allows the observation of shifts in the peaks of the $W_{19.8}Mo_{19.8}Nb_{19.8}Ti_{19.8}Cr_{19.8}Al_1$ (At. %) alloy to lower angles as milling time increases, indicating solubilization of the elements in the BCC lattice.

After milling for 12, 24, 36, and 48 hours, the lattice constant was measured as 3.162, 3.159, 3.165, and 3.145 Å, respectively. It is important to note that variations in the lattice parameter values are attributed not only to the inter-diffusion of Mo, Nb, Ti, Cr, and W forming a BCC phase but also to the influence of the amorphization process, which induces crystalline lattice distortion. Both factors contribute to changes in lattice parameters.

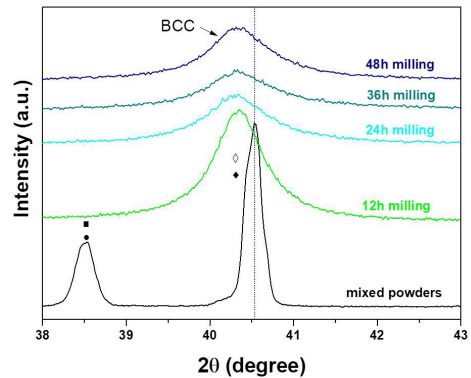To substantiate these statements, diffraction refinement was conducted after 12, 24, 36, and 48 hours of milling

time using the Rietveld method, as shown in Figure 6. After 12 hours of milling (Figure 6b), the predominant peaks form a solid solution characterized by BCC structure (containing W, Mo, Nb, Ti). This phase has a volume fraction of 84 Vol%. Other minor BCC contain Cr, constituting a smaller fraction of 16 Vol%.

With increase in milling time for 24 hours, observed stabilization in the BCC phase corresponding W element (Figure 6c) the volume fraction of the main BCC phase was 85.5 Vol. % and the minor BCC 14.5 Vol %. After 36 hours of milling (Figure 6d), the volumetric fraction corresponding to the main BCC increases significantly to 96.6 Vol%, while the proportion of minor BCC decreases to 3.4 Vol%, and after milling time of 48 hours (Figure 6e) the minor BCC-related peak is imperceptible, leaving only BCC solid solution peaks. This observation indicates the homogenization and inter-diffusion of all elements after 48 hours of milling.

3.4. Williamson-Hall plot

The Williamson-Hall (W-H) plot has been widely applied for the calculation of crystallite size and strain in crystalline materials. This method evaluates the defects in the lattice, such as, point, line, area defects, etc[41].

The following equations describe the Scherrer Equation 1, which calculates the crystallite size, and the Stokes and Wilson Equation 2, which represents the strain in the crystal. From both, we can obtain Equation 3, in which cos (θ) is related to the crystallite size and tan (θ) is related to the microstrain[41].

Equation 3 depicts the W-H uniform stress model, where D represents crystallite size, K is the radiation wavelength (Cu-Kα), h is the Bragg reflection angle, K stands for the form factor of the crystalline domain with a value of 0.94, and B represents the Full Width at Half Maximum (FWHM). It is worth noting that this equation assumes uniform stress within the lattice, which does not accurately describe the behavior of ball-milled powders[42].

To address this limitation, an alternative approach was adopted, known as the Uniform Stress Deformation Model (USDM), which considers the anisotropic nature of material deformation. If strain is uniformly distributed the Equation 4 is applied to compute the crystallite size and strain in the
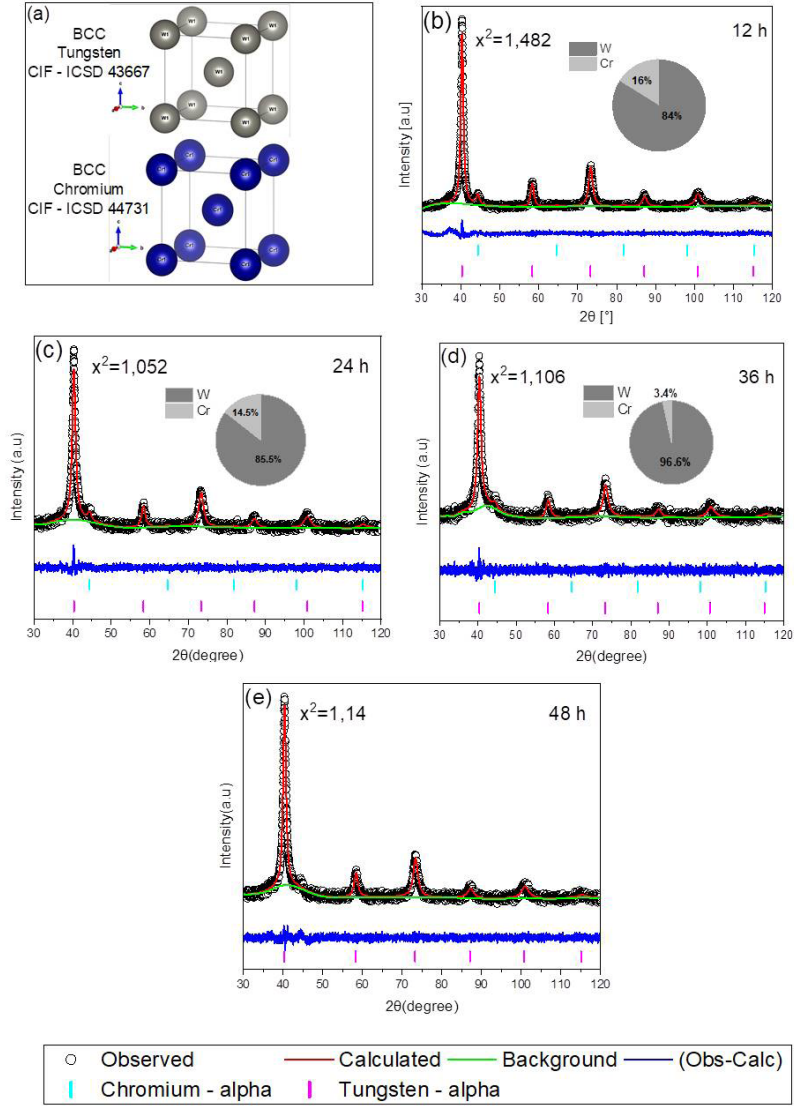
Development of Multi-Principal Element Alloys $W_{19.8}Mo_{19.8}Nb_{19.8}Ti_{19.8}Cr_{19.8}Al_1$ (At. %) Through Mechanical Alloying Process

7

Figure 6. Rietveld refinement of the $W_{19.8}Mo_{19.8}Nb_{19.8}Ti_{19.8}Cr_{19.8}Al_1$ (At. %) alloy after b) 12, c) 24, d) 36 and e) 48 hours milling time.

crystals, the Equation 4 can be from Equation 3 if to multiply both size by cos (θ) the transition from the Williamson-Hall (W-H) model to the USDM. In this modified model, lattice deformation (ε) replaces stress (σ), adhering to Hooke's Law ($\sigma = E_{hkl\varepsilon}$).

$$B = \frac{K\lambda}{D\cos(\theta)} \quad (1)$$

$$B \text{ strain} = 4\varepsilon \tan(\theta) \quad (2)$$

$$B = \frac{k\lambda}{D\cos(\theta)} + 4\varepsilon \tan(\theta) \quad (3)$$

$$B\cos(\theta) = \frac{k\lambda}{D} + \frac{4\sigma\sin(\theta)}{E_{hkl}} \quad (4)$$

To cubic crystals, Young modulus, E_{hkl}, is given in Equation 5:

$$\frac{1}{E_{hkl}} = S_{11} - 2\left(S_{11} - S_{12} - \frac{1}{2}S_{44}\right)\left(\frac{h^2k^2 + k^2l^2 + l^2h}{h^2 + k^2 + l^2}\right) \quad (5)$$

S_{11}, S_{12}, and S_{44} are elastic compliances, and the values for W are $S_{11} = 2.6 \times 10^{-12}$ Pa, $S_{12} = -0.7 \times 10^{-12}$ Pa, and $S_{44} = 6.6 \times 10^{-12}$ Pa[43] and the values for Cr are $S_{11} = 3.056 \times 10^{-12}$ Pa, $S_{12} = -0.5 \times 10^{-12}$ Pa, and $S_{44} = 9.9 \times 10^{-12}$ Pa[44].

Figure 7 shows the plot of the W-H method between Bcos(θ) and 4sin(θ)/Y_{hkl} for the mixed powders (0 hour) 12, 24, 36, and 48 hours of milling, where the intercept of the plot was used to calculate the crystallite size. This method has been calculated from the Uniform Stress Deformation Model (USDM)[37].
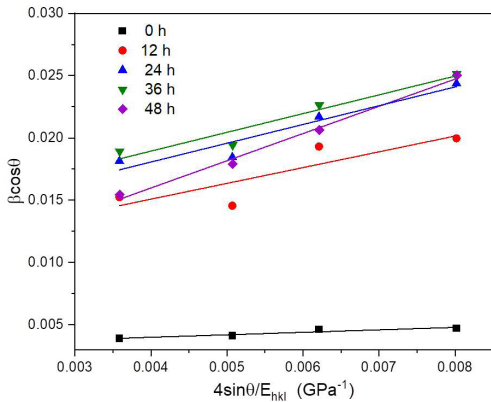
Figure 7. Uniform stress deformation model (Williamson-Hall plot) for $W_{19.8}Mo_{19.8}Nb_{19.8}Ti_{19.8}Cr_{19.8}Al_1$ (At. %) alloy, milled for 0, 12, 24, 36 and 48 hours.
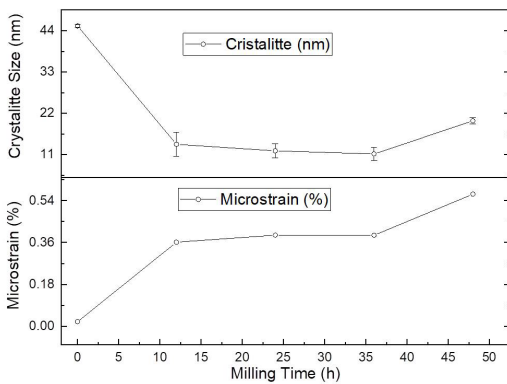

Figure 8. Particle size and microstrain (ε) for 12, 24, 36 and 48h milling time.

Figure 8 depicts the evolution of crystallite size and microstrain (ε) over milling time. For the mixed powders (0 hours), there is not a microstrain, and the crystallite size is around 44 nm. After 12 hours of milling, there is a noted increase in microstrains (0.34%) and a decrease in crystallite size (~12.5 nm). Between 24 and 36 hours of milling, the crystallite size decreases from 12.03 to 11.21 nm, while the microstrain undergoes marginal changes from 0.3917 to 0.3914%, indicating slight strain or distortion within the crystallites caused by high deformation placed from milling. Contrastingly, after 48 hours of milling, there is an increase in both crystallite size to 20 nm and microstrain to 0.568%.

The explanation for these increments in crystallite and microstrain is that during mechanical milling, high energy is introduced into the alloy, and this energy can be stored in the alloy grain boundaries and/or atomic disorder. In cases of atomic disorder, milling can introduce a high density of point defects, such as vacancies and anti-site defects, and assist the diffusive processes in achieving structure reordering[17].

4. Conclusions

In the present study, the $W_{19.8}Mo_{19.8}Nb_{19.8}Ti_{19.8}Cr_{19.8}Al_1$ (At. %) alloy was produced via mechanical alloying (MA) to investigate particle characteristics and crystallite size at three different milling durations: 24, 36, and 48 hours. The investigation employed SEM/BSE, XRD, Rietveld refinement, and the W-H method. The findings can be summarized as follows:

- Thermocalc results assisted in the identification of phases such as BCC $W_{19.8}Mo_{19.8}Nb_{19.8}Ti_{19.8}Cr_{19.8}Al_1$ (At. %) alloy to be above 2000 °C, with BCC stabilization at elevated temperatures.
- The particle size analysis conducted using ImageJ software revealed particle sizes consistent with the SEM micrographs, indicating smaller particle sizes for both milling times. Conversely, laser granulometric analysis allows for more extensive sampling, resulting in a higher particle count and leading to discrepancies in the granulometric results.
- The XRD analysis shows as the milling time increased from 12 to 48 hours, the elements such as, Mo, Nb, Ti, Cr and Al tended to incorporate into in the W element lattice forming only BCC phase and the Rietveld refinement corroborated with this results, with the volumetric fraction of the BCC phase increase from 84 to 100 Vol. %.
- The EDS shows high contamination by Fe, especially for longer milling times, such as 36 and 48 hours (28 and 21 At.%,), respectively, for shorter times, 12h there was less contamination in the order of 9 At.%. These impurities comes from milling balls and bowl, as well as, the parameters adopted in this work as high BPR (15:01) and speed rotation of the 400 rpm.
- The W-H method revealed a gradual decrease in crystallite size to 0 to 12 hours of milling and a microstrain increase to 0 from 0.34, resulting in plastic deformation. After 24 and 36 hours, the crystallite size tends to decrease and microstrain from 24 to 36 hours, indicating an amorphous characteristic. Conversely, from 36 to 48 hours, both parameters increased, suggesting a structure reordered during this milling duration.

5. References

1. Murty BS, Yeh J-W, Ranganathan S, Bhattacharjee P. High-entropy alloys. Amsterdam: Elsevier; 2019. http://doi.org/10.1016/B978-0-12-816067-1.00010-2.
2. Gao MC, Yeh J-W, Liaw PK, Zhang Y. High-entropy alloys. Switzerland: Springer International Publishing; 2016. http://doi.org/10.1007/978-3-319-27013-5.
3. Coury FG, Kaufman M, Clarke AJ. Solid-solution strengthening in refractory high entropy alloys. Acta Mater. 2019;175:66-81. http://doi.org/10.1016/j.actamat.2019.06.006.
4. Vaidya M, Muralikrishna GM, Murty BS. High-entropy alloys by mechanical alloying: a review. J Mater Res. 2019;34(5):664-86. http://doi.org/10.1557/jmr.2019.37.
5. Raghavan R, Hari Kumar KC, Murty BS. Analysis of phase formation in multi-component alloys. J Alloys Compd. 2012;544:152-8. http://doi.org/10.1016/j.jallcom.2012.07.105.
6. Gorsse S, Couzinié JP, Miracle DB. From high-entropy alloys to complex concentrated alloys. C R Phys. 2018;19(8):721-36. http://doi.org/10.1016/j.crhy.2018.09.004.
7. Kilmametov A, Kulagin R, Mazilkin A, Seils S, Boll T, Heilmaier M, et al. High-pressure torsion driven mechanical alloying of

Development of Multi-Principal Element Alloys W$_{19.8}$Mo$_{19.8}$Nb$_{19.8}$Ti$_{19.8}$Cr$_{19.8}$Al$_1$ (At. %) Through Mechanical Alloying Process

9

CoCrFeMnNi high entropy alloy. Scr Mater. 2019;158:29-33. http://doi.org/10.1016/j.scriptamat.2018.08.031.

8. Pickering EJ, Jones NG. High-entropy alloys: a critical assessment of their founding principles and future prospects. Int Mater Rev. 2016;61(3):183-202. http://doi.org/10.1080/09506608.2016.1180020.

9. Cantor B. Multicomponent and high entropy alloys. Entropy. 2014;16(9):4749-68. http://doi.org/10.3390/e16094749.

10. Xiang L, Guo W, Liu B, Fu A, Li J, Fang Q, et al. Microstructure and mechanical properties of TaNbVTiAl$_x$ refractory high-entropy alloys. Entropy. 2020;22(3):282. http://doi.org/10.3390/e22030282.

11. Senkov ON, Wilks GB, Scott JM, Miracle DB. Mechanical properties of Nb$_{25}$Mo$_{25}$Ta$_{25}$W$_{25}$ and V$_{20}$Nb$_{20}$Mo$_{20}$Ta$_{20}$W$_{20}$ refractory high entropy alloys. Intermetallics. 2011;19(5):698-706. http://doi.org/10.1016/j.intermet.2011.01.004.

12. Miracle DB, Senkov ON. A critical review of high entropy alloys and related concepts. Acta Mater. 2017;122:448-511. http://doi.org/10.1016/j.actamat.2016.08.081.

13. Senkov ON, Miracle DB, Chaput KJ, Couzinie J-P. Development and exploration of refractory high entropy alloys. J Mater Res. 2018;33(19):3092-128. http://doi.org/10.1557/jmr.2018.153.

14. Raman L, Guruvidyathri K, Kumari G, Murty SVSN, Kottada S, Murty BS. Phase evolution of refractory high-entropy alloy CrMoNbTiW during mechanical alloying and spark plasma sintering. J Mater Res. 2019;34(5):756-66. http://doi.org/10.1557/jmr.2018.483.

15. Zhang P, Li Y, Chen Z, Zhang J, Shen B. Oxidation response of a vacuum arc melted NbZrTiCrAl refractory high entropy alloy at 800-1200 °C. Vacuum. 2019;162:20-7. http://doi.org/10.1016/j.vacuum.2019.01.026.

16. Oleszak D, Antolak-dudka A, Kulik T. High entropy multicomponent WMoNbZrV alloy processed by mechanical alloying. Mater Lett. 2018;232:160-2. http://doi.org/10.1016/j.matlet.2018.08.060.

17. Suryanarayana C. Mechanical alloying and milling. Prog Mater Sci. 2001;46(1-2):1-184. http://doi.org/10.1016/S0079-6425(99)00010-9.

18. Naghiha H, Movahedi B, Asadabad MA, Mournani MT. Amorphization and nanocrystalline Nb3Al intermetallic formation during mechanical alloying and subsequent annealing. Adv Powder Technol. 2017;28(2):340-5. http://doi.org/10.1016/j.apt.2016.09.022.

19. Qiao Y, Tang Y, Li S, Ye Y, Liu X, Zhu L, et al. Preparation of TiZrNbTa refractory high-entropy alloy powder by mechanical alloying with liquid process control agents. Intermetallics. 2020;126:106900. http://doi.org/10.1016/j.intermet.2020.106900.

20. German RM. Powder metallurgy science. 2nd ed. Princeton: Metal Powder Industries Federation; 1994.

21. Lv S, Zu Y, Chen G, Zhao B, Fu X, Zhou W. A multiple nonmetallic atoms co-doped CrMoNbWTi refractory high-entropy alloy with ultra-high strength and hardness. Mater Sci Eng A. 2020;795:140035. http://doi.org/10.1016/j.msea.2020.140035.

22. Liu X, Cheng H, Li Z, Wang H, Chang F, Wang W, et al. entropy alloy produced by mechanical alloying and vacuum hot pressing sintering. Vacuum. 2019;165:297-304. http://doi.org/10.1016/j.vacuum.2019.04.043.

23. Bhardwaj V, Zhou Q, Zhang F, Han W, Du Y, Hua K, et al. Effect of Al addition on the microstructure, mechanical and wear properties of TiZrNbHf refractory high entropy alloys. Tribol Int. 2021;160:107031. http://doi.org/10.1016/j.triboint.2021.107031.

24. Ge S, Fu H, Zhang L, Mao H, Li H, Wang A, et al. Effects of Al addition on the microstructures and properties of MoNbTaTiV refractory high entropy alloy. Mater Sci Eng A. 2020;784:139275. http://doi.org/10.1016/j.msea.2020.139275.

25. Soni V, Senkov ON, Couzinie JP, Zheng Y, Gwalani B, Banerjee R. Phase stability and microstructure evolution in a ductile refractory high entropy alloy Al$_{10}$Nb$_{15}$Ta$_5$Ti$_{30}$Zr$_{40}$. Materialia. 2020;9:100569. http://doi.org/10.1016/j.mtla.2019.100569.

26. Müller F, Gorr B, Christ HJ, Chen H, Kauffmann A, Laube S, et al. Formation of complex intermetallic phases in novel refractory high-entropy alloys NbMoCrTiAl and TaMoCrTiAl: thermodynamic assessment and experimental validation. J Alloys Compd. 2020;842:155726. http://doi.org/10.1016/j.jallcom.2020.155726.

27. Thermo-Calc Software [homepage on the Internet]. 2014 [cited 2023 Dec 13]. Available from: www.thermocalc.com

28. Zhu M, Yao L, Liu Y, Zhang M, Li K, Jian Z. Microstructure evolution and mechanical properties of a novel CrNbTiZrAlx (0.25 ≤ x ≤ 1.25) eutectic refractory high-entropy alloy. Mater Lett. 2020;272:127869. http://doi.org/10.1016/j.matlet.2020.127869.

29. Qiao Y, Tang Y, Li S, Ye Y, Liu X, Zhu L, et al. Preparation of TiZrNbTa refractory high-entropy alloy powder by mechanical alloying with liquid process control agents. Intermetallics. 2020;126:106900. http://doi.org/10.1016/j.intermet.2020.106900.

30. Long Y, Su K, Zhang J, Liang X, Peng H, Li X. Enhanced strength of a mechanical alloyed NbMoTaWVTi refractory high entropy alloy. Materials. 2018;11(5):6. http://doi.org/10.3390/ma11050669.

31. Pan J, Dai T, Lu T, Ni X, Dai J, Li M. Microstructure and mechanical properties of Nb$_{25}$Mo$_{25}$Ta$_{25}$W$_{25}$ and Ti$_8$Nb$_{23}$Mo$_{23}$Ta$_{23}$W$_{23}$ high entropy alloys prepared by mechanical alloying and spark plasma sintering. Mater Sci Eng A. 2018;738:362-6. http://doi.org/10.1016/j.msea.2018.09.089.

32. Gao F, Sun Y, Hu L, Shen J, Liu W, Ba M, et al. Microstructural evolution and thermal stability in a nanocrystalline lightweight TiAlV$_{0.5}$CrMo refractory high-entropy alloy synthesized by mechanical alloying. Mater Lett. 2022;329:133179. http://doi.org/10.1016/j.matlet.2022.133179.

33. Kalantari H, Khayati GR, Adeli M. A high entropy alloy of AlCrFeNiTiZn synthesized through mechanical alloying and sintering. Intermetallics. 2023;161:107981. http://doi.org/10.1016/j.intermet.2023.107981.

34. Yan J, Li M, Li K, Qiu J, Guo Y. Effects of Cr content on microstructure and mechanical properties of WMoNbTiCr high-entropy alloys. J Mater Eng Perform. 2020;29(4):2125-33. http://doi.org/10.1007/s11665-020-04744-7.

35. Kraus W, Nolze G. Powder cell-a program for the representation and manipulation of crystal structures and calculation of the resulting x-ray powder patterns. J Appl Cryst. 1996;29(3):301-3. http://doi.org/10.1107/S0021889895014920.

36. Villars P, Cenzual K. Pearsonas crystal data: crystal structure database for inorganic compounds. Materials Park: ASM International; 2007.

37. Sivakumar M, Dasgupta A, Ghosh C, Sornadurai D, Saroja S. Optimisation of high energy ball milling parameters to synthesize oxide dispersion strengthened Alloy 617 powder and its characterization. Adv Powder Technol. 2019;30(10):2320-9. http://doi.org/10.1016/j.apt.2019.07.014.

38. Villars P, Calvert L. Pearson's handbook of crystallographic data for intermetallic phases. 2nd ed. Materials Park: ASM International; 1991.

39. Sarkar A, Srinivasan A, Robi PS. Processing and characterization of TiNbMoTaW refractory high entropy alloy by mechanical alloying. Adv Powder Technol. 2023;34(12):104276. http://doi.org/10.1016/j.apt.2023.104276.

40. Zhan L, Hou J, Wang G, Chen Y, Luo S, Kang Q, et al. Study on mechanical alloying behavior and thermal stability of HfMoNbTaTi refractory high-entropy alloy. Mater Charact. 2023;203:113122. http://doi.org/10.1016/j.matchar.2023.113122.

41. Sahadat Hossain M, Ahmed S. Easy and green synthesis of TiO$_2$ (Anatase and Rutile): estimation of crystallite size using Scherrer equation, Williamson-Hall plot, Monshi-Scherrer Model, size-strain plot, Halder- Wagner model. Results in Materials. 2023;20:100492. http://doi.org/10.1016/j.rinma.2023.100492.

42. Saravanan MS, Sivaprasad K, Susila P, Babu SK. Anisotropy models in precise crystallite size determination of mechanically

alloyed powders. Physica B. 2011;406(2):165-8. http://doi.org/10.1016/j.physb.2010.10.023.

43. Dieter GE. Mechanical metallurgy. London: Grawhill Book Company; 2005.

44. Boulanger PH, Hayes M. Bounds on the extensional strains in elastic homogeneous crystals under simple tension. IMA J Appl Math. 2007;72(5):577-96. http://doi.org/10.1093/imamat/hxm030.